Journal Pre-proof

Characterization of the Gas Tungsten Arc Welding (GTAW) joint of Armco iron nanostructured by Equal-Channel Angular Pressing (ECAP)

Jairo Alberto Muñoz (Investigation) (Formal analysis) (Writing - original draft) (Writing - review and editing), Alexander Komissarov (Supervision)<ce:contributor-role>fundIng acquisition) (Investigation), Ignacio Mejía (Supervision) (Formal analysis) (Methodology), Humberto Hernández-Belmontes (Investigation) (Methodology) (Funding acquisition), José-María Cabrera (Supervision) (Writing - review and editing) (Resources) (Project administration) (Funding acquisition) (Data curation)

Please cite this article as: Muñoz JA, Komissarov A, Mejía I, Hernández-Belmontes H, Cabrera J-María, Characterization of the Gas Tungsten Arc Welding (GTAW) joint of Armco iron nanostructured by Equal-Channel Angular Pressing (ECAP), *Journal of Materials Processing Tech.* (2020), doi: https://doi.org/10.1016/j.jmatprotec.2020.116902

Characterization of the Gas Tungsten Arc Welding (GTAW) joint of Armco iron nanostructured by Equal-Channel Angular Pressing (ECAP)

Jairo Alberto Muñoz[1, 2, a,*], Alexander Komissarov [1, b], Ignacio Mejía [3, c], Humberto Hernández-Belmontes [3, d], José-María Cabrera [3, 4, e]

[1] National University of Science and Technology "MISIS", Moscow 119049, Russia.
[2] Instituto de Física Rosario, Consejo Nacional de Investigaciones Científicas y Técnicas-CONICET, Universidad Nacional de Rosario, Ocampo y Esmeralda, 2000 Rosario, Argentina.
[3] Research Institute in Metallurgy and Materials, Universidad Michoacana de San Nicolás de Hidalgo, Edificio "U-3", Ciudad Universitaria, 58030-Morelia, Michoacán, Mexico.
[4] Department of Materials Science and Engineering EEBE, Universidad Politécnica de Catalunya, c/Eduard Maristany 10-14, 08019 Barcelona, Spain.

*corresponding author: munos.bk@misis.ru

[a] munos.bk@misis.ru, [b] komissarov@misis.ru, [c] imejia@umich.mx, [d] monsches886@gmail.com, [e] jose.maria.cabrera@upc.edu.

Graphical abstract
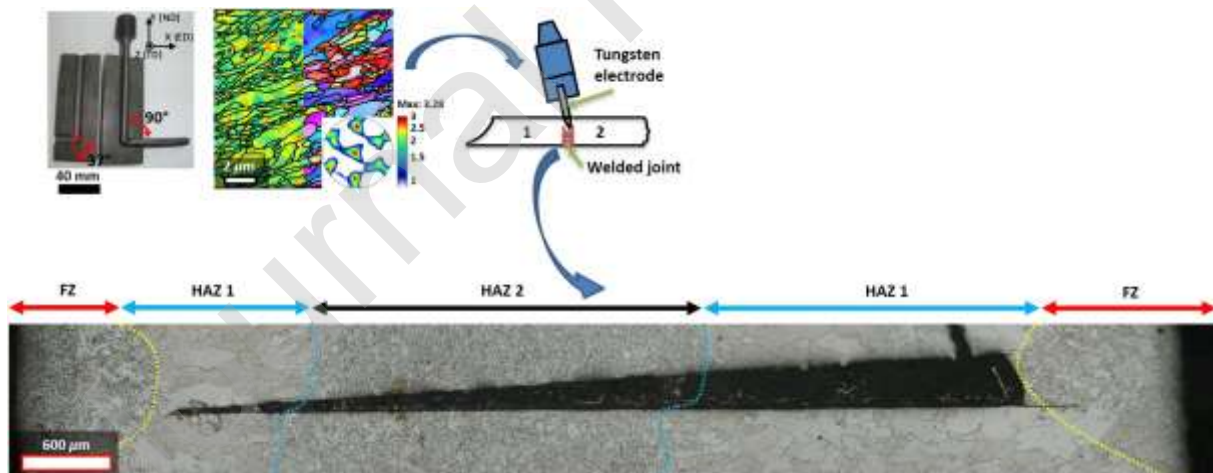
Highlights

- Ultrafine-grained Armco iron was obtained by severe plastic deformation and submitted to welding.
- Gas Tungsten arc welding generates a gradient microstructure as a function of the heat input.
- Hardness decreases after the welding process but still superior to the annealed material.
- High heat inputs generate the formation of Widmanstätten ferrite.

Abstract

After Severe Plastic Deformation (SPD), the strength of the Armco iron sharply increases with the number of Equal-Channel Angular Pressing (ECAP) passes. So, the ultimate tensile stress (UTS) reached up to 800 MPa after eight passes, reflecting an increment of around four times than the as-received material strength. The original grain size of the annealed iron of about 70 μm also experimented with drastic changes after ECAP, reaching grain sizes approaching to 300 nm. Samples were then welded by the Gas Tungsten Arc Welding (GTAW) process varying the voltage and current conditions. Metallographic analysis by Light Optical Microscopy (LOM) and Electron Backscatter Diffraction (EBSD), was carried out to analyze the weld penetration, Fusion Zone (FZ), and the size and microstructure morphology across the Heat Affected Zone (HAZ). Special attention was given to microstructure changes of the nanostructured base metal. A microstructural gradient was observed throughout the welded joint with hardness reduction concerning the nanostructured material but still superior to the material without ECAP. The temperature heterogeneity gave rise to different grain sizes and morphologies like Widmanstätten ferrite around the FZ, especially at high heat inputs.

1   Introduction

According to Murugan et al. (2001) weldability profoundly circumscribes the utilization of steel as structure material. This requirement is particularly true in the automotive industry where the application of advance high-strength steels (AHSS) must be coupled with weldability. Most new AHSS achieve their mechanical properties by a careful combination of

the chemical compositions and an appropriated thermomechanical processing. In general, these steels have some significant alloying amounts in contrast with classical structural steels. This behavior, in turn, promotes weldability problems, so alloying is maintained at the minimum level need to accomplish the desired performance. Consequently, it is of considerable importance to augment welding efficiency without sacrificing the performance of the welded joint. However, in many AHSS, such as in Dual Phase (DP), Transformed Induced Plasticity (TRIP), Complex Phase (CP) or Quench and Partitioning (QP) steels, the desired microstructure (ferrite-martensite, ferrite-bainite-martensite, bainite-martensite-pearlite-retained austenite, and martensite-retained austenite, respectively) losses its characteristics constituents after a welding operation. Nevertheless, the total chemical content ensures that in the FZ or the HAZ, no fully martensitic microstructures appear. Therefore, these steels are considered as weldable under certain processing parameters.

One possible alternative to reach very high strength while keeping a very good weldability is the obtention of iron-base alloys with grain sizes in the order of a few hundreds of nanometers. In particular, one plausible candidate to reach such a requirement is an Armco iron nanostructured by SPD techniques like ECAP. ECAP is a promising technique to fabricate ultrafine grain microstructures. Bagherpour et al. (2019) demonstrated the constantly growing interest of the scientific community to develop new SPD techniques, and Valiev et al. (2010) showed the superior strength obtained by metallic materials with ultrafine microstructures. However, that kind of microstructures makes the materials have a limit for their use, since it has been proved that SPD can increase the strength of the metallic materials, but, at the same time, it diminishes their ductility. Huang and Langdon (2013) established that this balance in mechanical properties is because, throughout large plastic deformations, the original coarse grain structure transforms into a microstructure on a very small scale handicapping the free movement of dislocations. On the other hand, Muñoz et al. (2017b) demonstrated that ultrafine Armco iron presented better high cycle fatigue strength than the coarse grain condition.

Moreover, the nanometric size of the microstructure of metals achieved after SPD at room temperature can be highly unstable due to the high internal energy state. This makes a real challenge to maintain all those excellent properties when they are heat treated or hot worked. For instance, Yoda et al. (2011) found that the tensile strength of ultrafine interstitial-free (IF) steel manufactured by accumulative roll-bonding decreases after annealing treatments at temperatures higher than 600 °C, while Ko and Hamad (2018) reported good thermal stability for low carbon steel deformed by differential speed rolling and subsequent annealing treatments

at 500 °C and different holding times. Since commercially pure iron presents an inherent excellent weldability, the study of its behavior in the ultrafine grain state at high temperatures may change due to the high temperature cycles involved during welding processes.

In most welding processes, high temperatures are involved, as well as temperature gradients that can significantly modify the Base Material (BM) properties due to the appearance of microstructural recovery, recrystallization, and grain growth phenomena. Temperature gradients give rise to a material with mechanical and microstructural properties that can vary considerably over the weldment dimensions. Wang et al. (2017) obtained different hardness values across the FZ and the HAZ due to the formation of columnar grains in the FZ.

Among the different fusion welding processes currently in existence, the Gas Tungsten Arc Welding (GTAW) process is characterized by producing high-quality welds (more resistant and high integrity) in all metals and alloys due to the greater control that the operator has over the process compared to other welding methods. Besides, it is a process that can operate with direct current (DC), as well as alternating current (AC). GTAW, due to the protection shield generated by argon or helium, is also considered as a clean process as demonstrated by Lathabai (2011). Although, according to Messler Jr (1999) the biggest limitation of this process lies in the low deposition rate when using filler material.

In the GTAW process, the different parameters involved, such as voltage, heat input, current, time, among others, have a huge impact on the final material properties. Owunna et al. (2018) showed that the higher the degree of penetration of the weld bead, the better the resistance and load capacity of the welded joint. They also found that the higher the temperature distribution, the broader the HAZs. Welding processes generate significant variations in grain size and hardness between the neighborhoods of the weld joint and the furthest areas. Yousefieh et al. (2011) analyzed the impact of the GTAW process heat input on the corrosion resistance and microstructural changes of duplex stainless steel finding the best corrosion properties for heat inputs around 0.95 kJ/mm. Conversely, Yang et al. (2011) pointed out that high heat inputs improved the low-temperature toughness and decreased the corrosion endurance of duplex stainless steel as a consequence of the Widmanstätten austenite formation. One of the critical positive points in weld joints is that the mechanical properties after the process should not substantially diminish concerning the base material. For instance, Singh et al. (2020) found variations in hardness at different distances from the weld joint between a stainless steel and copper by GTAW with good overall mechanical behavior.

The purpose of this research is the examination of the microstructure changes and thermal stability of severely deformed commercially pure Armco iron in the as-weld condition using GTAW at different welding conditions (voltage, current, and time). For this reason, grain size evolution and hardness measurements were carried out throughout the entire welded joint. Additionally, the thermal stability of the material was carried out through heat treatment cycles with high heating and cooling rates by dilatometry and subsequent study of the microstructure by EBSD. One relevant aspect is that nowadays, weldability studies of nanostructured metallic materials are scarce, almost non-existent. Therefore, the research of nanostructured materials welding properties opens up a new study field that requires attention from the scientific community.

2   Experimental procedure

Table 1 presents the chemical composition of the material. A commercial Armco iron was received in the form of 8 mm diameter and 60 mm length rods. Before pressing, samples were heat-treated at 930 °C for 20 minutes and air cooled. For the ECAP process, a die with interior and exterior angles of 90° and 37°, respectively, was manufactured, as indicated in Fig. 1(a). ECAP processing was carried out at room temperature using a hydraulic press with 80 tons capacity with a pressing rate of 10 mm/s. The material was processed until 8 ECAP passes (ultrafine-grained state) following the B_C route (i.e., 90° clockwise rotation around the longitudinal axis between each ECAP pass). To minimize friction effects, Molybdenum disulfide (MoS_2) was used. The reason for selecting 8 passes is based on the fact that the microstructure is not any more refined beyond 8 ECAP passes, and an equilibrium microstructure is attained no matter if further ECAP passes are given, as shown in Muñoz (2019).

Tensile tests were performed at room temperature with a strain rate of 5.5×10^{-4} s^{-1}. Vickers hardness measurements in each zone across the sample diameter were obtained with 0.91N load and dwell time 10 s.

Table 1. Chemical composition of Armco iron.

Element	C	Si	Mn	P	S	Cr	Mo	Ni	Al	Fe
wt %	0.01	0.01	0.06	<0.01	<0.01	0.02	<0.005	0.038	0.013	Balance

Samples with 8 ECAP passes were cut throughout the diameter and then welded by the GTAW process (Fig. 1(b)) in butt joints (no filler material was added). Three welding conditions (current intensity I, voltage V and time t) were analyzed: I= 100 A, V= 8 v, t= 45 s (100A-8V-45s); I= 125 A, V= 10 v, t= 45 s (125A-10V-45s); and I= 150 A, V= 10 v, t= 45 s (150A-10V-45s). An Ar gas protection flow rate of 15 l/min was used. The GTAW process set up was 60° vertex angle and 2.4 mm in diameter thoriated tungsten electrode. After the welding process, samples from the transversal direction plane of the welded samples were extracted and etched with Nital 2% (2ml HNO_3 + 98ml C_2H_5OH) reagent to reveal the microstructural changes around the welded zone. In this way, the FZ, HAZ, and BM were examined under an optical microscope. ImageJ software was employed to calculate grain sizes distributions across the welded joints following the algorithm proposed by Igathinathane et al. (2008).
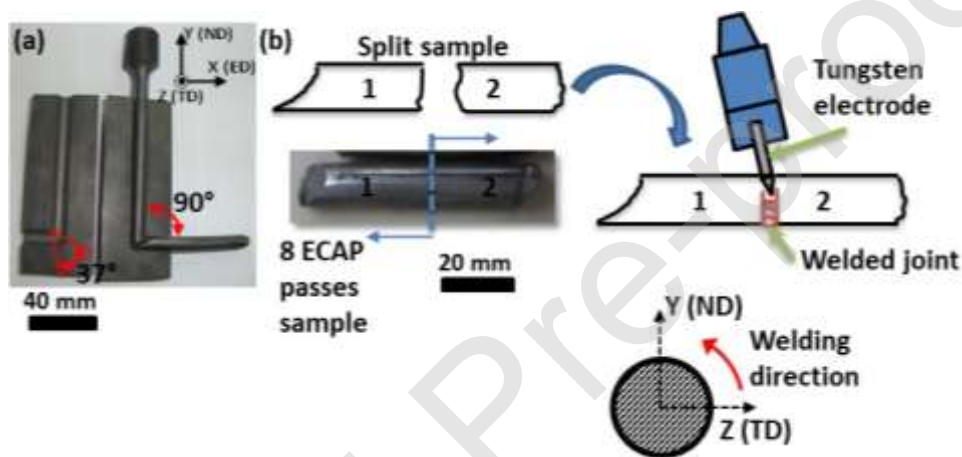

Fig. 1. (a) ECAP die set up, and (b) welding process description for the 8 ECAP passes material.

Electron Backscattered Diffraction (EBSD) and Light Optical Microscopy (LOM) techniques were employed to measure the microstructural properties. Samples were analyzed on the transverse direction (TD) plane. The data were analyzed with TSL OIM 7.3b and MTEX software. Misorientations larger than 15° were used to define grain boundaries, while subgrains were identified with misorientations between 2° and 15°. Geometrically Necessary Dislocations (GND) densities were quantified from the EBSD maps through the MTEX software (Bachmann et al., 2010).

In order to simulate the welding temperatures and material thermal stability, fast heating rate tests were carried out on ECAP-processed billets. These tests were performed on a computer-controlled dilatometer DIL805 thermomechanical simulator. Thermal cycles consist

of heating up to 950 °C and 1150 °C for 2 s using fast heating rates of 3000-4000 °C/s. After heating, samples were cooled down at high rates under argon atmosphere.

3 Results and discussion

3.1 Material characterization

Fig. 2 summarizes the microstructure, texture, and tensile test curves for both the initial and 8 ECAP passes material. Fig. 2(a) displays the initial annealed condition: a microstructure with equiaxed grains, a low density of GNDs forming some walls with an average dislocation density value of $1.1 \cdot 10^{12}$ m^{-2}, and a typical rolling texture as demonstrated by the <110> pole figure although with low intensity. On the other hand, Fig. 2(b) shows the 8 ECAP passes sample: a less homogeneous grain structure as a consequence of the shearing strains generated by the material extrusion through the ECAP die, with high densities of GNDs forming walls and average dislocation density of $5.5 \cdot 10^{14}$ m^{-2}, indicating grains with high curvature and the potential to achieve further grain size reduction. Additionally, the material with 8 ECAP passes also presents a dissimilar texture from the initial material characterized by a twist around the transverse axis (~30 ° clockwise) following an ECAE type texture in agreement with ideal texture components described by Beyerlein and Tóth (2009).

The exceptional grain size reduction between the two conditions is evident in Fig. 2(c), with more than two magnitude orders, reducing from 71 μm to 0.38 μm after 8 ECAP passes at room temperature. Microstructural changes also occurred in the misorientation angle distributions, with two clearly defined behaviors, as indicated in Fig. 2(d). This latter figure allows concluding that the initial material presents high fractions of grain boundaries with high misorientations. At the same time, the ultrafine grain material displays a mixed behavior with misorientation peaks for angles lower than 15 ° but also a significant fraction of misorientations between 20 ° and 60 °. This behavior corroborates the texture evolution in which the initial material is closer to random than the severely deformed material.

The tensile behavior of the two materials recorded in Fig. 2(e) shows that the material with 8 ECAP passes increased its yield strength almost four times the initial material strength. However, the strength improvement was paid for with a clear reduction in its strain hardening ability relative to the initial material. In pure materials processed by SPD techniques, the ductility reduction is associated with the considerable increase of dislocations that give rise to the grain size fragmentation, which conducts to smaller grains that restrict the space for the free

movement of the dislocations. For that reason, Muñoz (2019) found high densities of dislocations (Statistical store and geometrically necessary dislocations) for ultrafine-grained Armco iron, while Muñoz et al. (2019) confirmed the high material strength. In any case, the total ductility of the material after ECAP is remarkable high (~ 0.2) although most of this ductility is displayed in the unstable region. Nevertheless, toughness, evaluated at a first glance as the energy absorbed before the fracture (area below the stress-strain curve) is significatively large in the SPD sample.
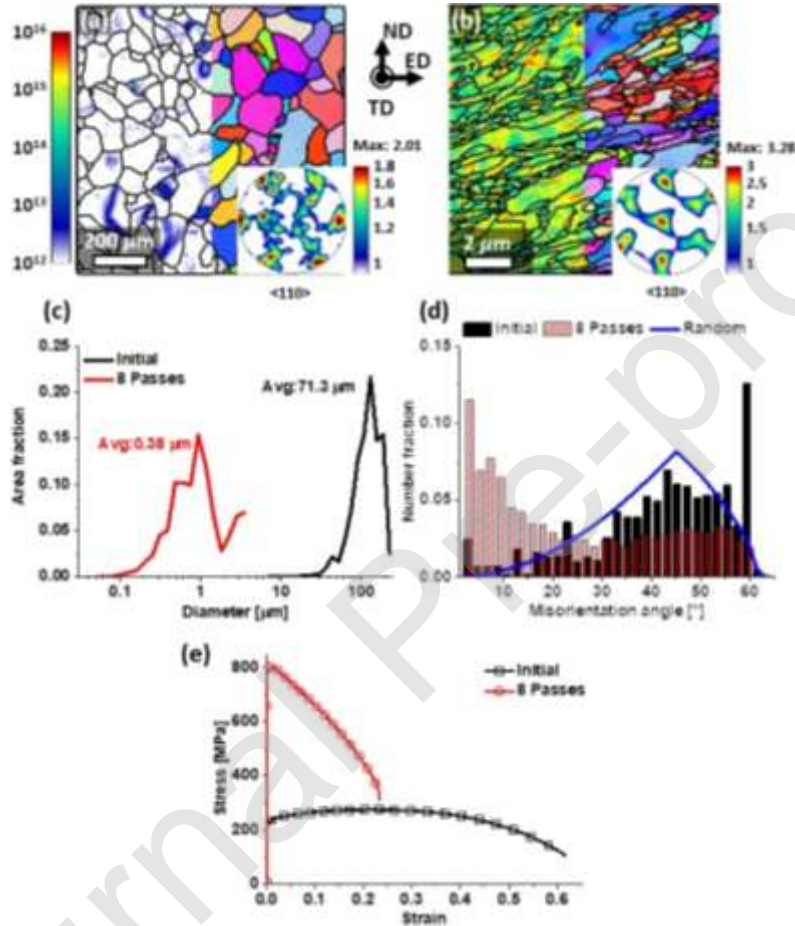

Fig. 2. Materials characterization (a) EBSD map (GND and IPF) and (110) pole figure for the initial annealed material, (b) EBSD map (GND and IPF) and (110) pole figure for the 8 ECAP passes material, (c) grain size comparison, (d) misorientation angle evolution of each condition, (e) tensile properties for both the initial and 8 ECAP passes materials.

3.2 Welding behavior

Figs. 3(a)-3(c) indicate the different zones generated during the welding process for the material deformed by ECAP after the different butt joint conditions tested. The first zone known as FZ is observed in a light color around the edge of the welded bar. Then the HAZ 1 appears, occupying a larger area that forms a darker semicircle around the FZ to end in the HAZ 2. This figure shows that the size of the FZ and HAZ 1 zones is larger on one side than on the other.

This behavior is due to the welding process's circumferential shape. Thus, the initial zone where the welding starts is again in contact when the entire perimeter of the sample is traveled, giving rise to a more significant thermal gradient on one side of the sample.
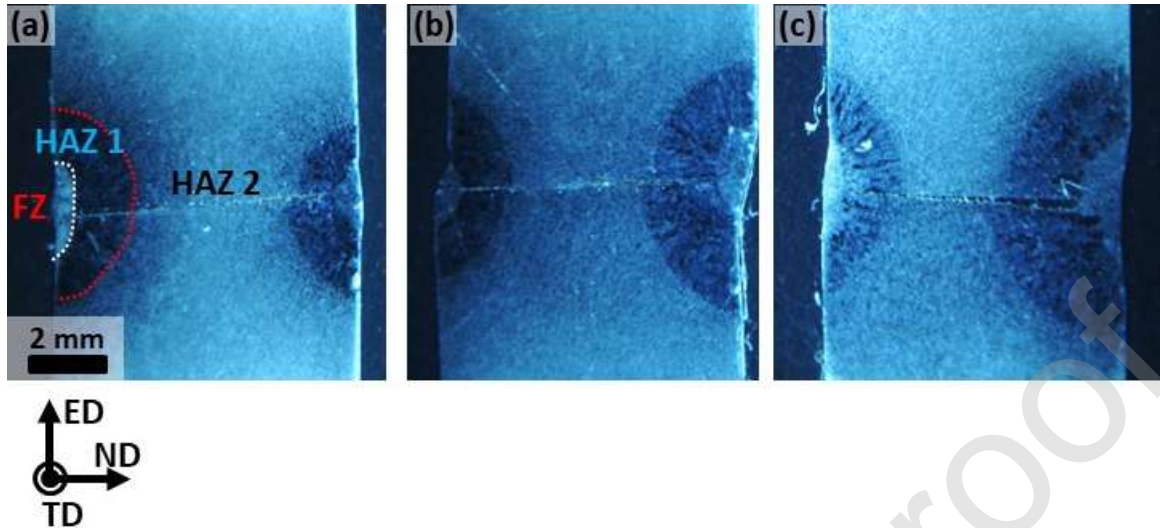

Fig. 3. Welded butt joints of the 8 ECAP passes sample at different conditions, (a) 100A-8V-45s, (b) 125A-10V-45s, and (c) 150A-10V-45s.

To appreciate the effects of the different welding conditions used in this study on the ultrafine grain material, Fig. 4-6 show the microstructural evolution along each of the welded joints described in Fig. 3(a)-3(c). Fig. 4(a) illustrates the microstructure evolution for condition 100A-8V-45s, where the existence of different types of morphology and grain sizes can be seen between the edges and the middle zone. Fig. 4(c) and Fig. 4(e) show how, in the HAZ 1, the grain size has grown abruptly concerning the middle zone (Fig. 4(d)) and certainly regarding the ultrafine grain material before being welded. It also highlights that in the middle zone, the morphology of the grains is more equiaxed (average ~28 µm) than in the edge vicinities (i.e., the FZ and HAZ 1) where the grains are elongated in the horizontal direction (average ~170 µm). There are also no major differences between FZ and HAZ 1, as indicated in Fig. 4(b).
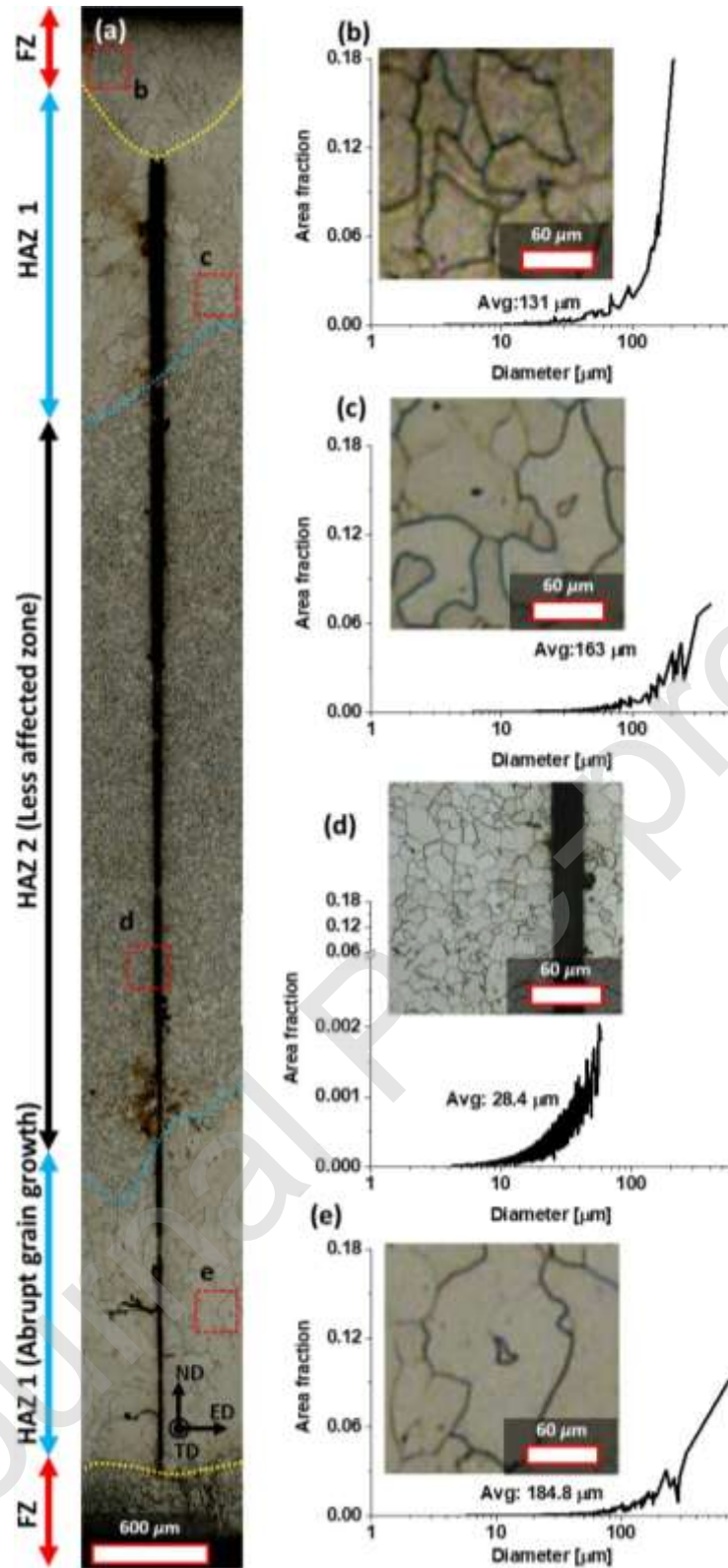
Fig. 4. Microstructure evolution for the 100A-8V-45s condition across the sample diameter, (a) microstructure evolution indicating the different zones after the welding process, (b) grain size values around the FZ, (c) grain size values around the HAZ 1, (d) grain size values around the HAZ 2, and (e) grain size values around the HAZ 1 (the amplified areas for figures 4(b), 4(c), 4(d), and 4(e) correspond with the red dash squares tagged with letters b, c, d, and e, respectively).
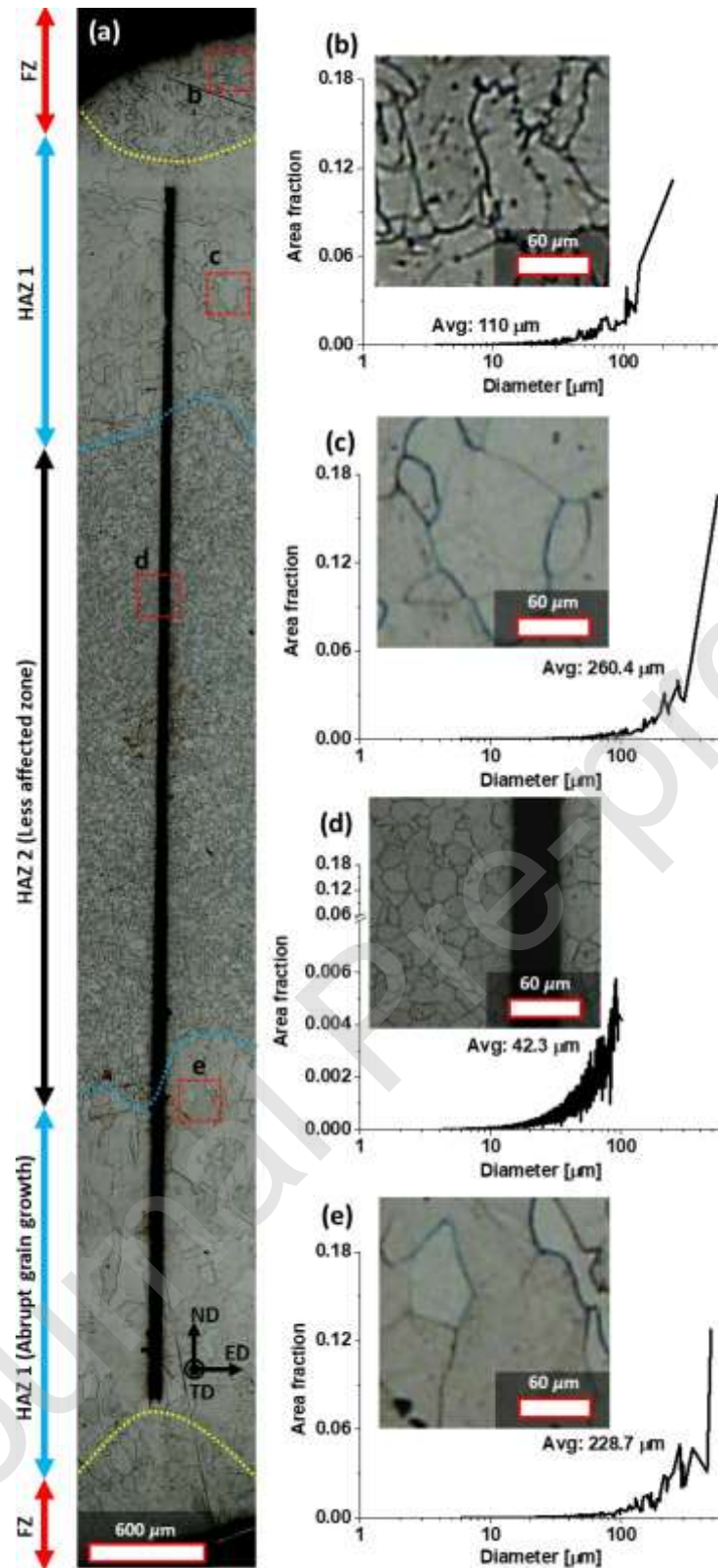
Fig. 5. Microstructure evolution for the 125A-10V-45s condition across the sample diameter, (a) microstructure evolution indicating the different zones after the welding process, (b) grain size values around the FZ, (c) grain size values around the HAZ 1, (d) grain size values around the HAZ 2, and (e) grain size values around the HAZ 1 (the amplified areas for figures 5(b), 5(c), 5(d), and 5(e) correspond with the red dash squares tagged with letters b, c, d, and e, respectively).

11

Fig. 5(a) demonstrates how increasing the current and voltage increases the size of the FZ, and HAZ 1 at the cost of reducing the HAZ 2. With the help of Fig. 5(c)-5(e), it is observed how the grain size in the HAZ 1 and HAZ 2 zones has grown concerning the 100A-8V-45s condition due to the high heat input related to the increased current flow. With a further increase in current to 150 A, Fig. 6(a) and Fig. 6(c)-6(e) show that the HAZ 2 has been reduced considerably from an extension of ~ 3975.9 μm in condition 100A-8V-45s to a length of ~ 2576.5 μm. Additionally, Fig 5(b) and Fig 6(b) highlights that in the FZ, particularly around the edges, new ferrite grains have nucleated with a morphology and size which differs from those observed in the other two conditions. These grains present an irregular feather-like shape with a grain size smaller than that of the HAZ. According to Gharibshahiyan et al. (2011) the different microstructural changes induced by each welding process connects to the temperature magnitude reached in each condition as well as the temperature gradient generated along the diameter of the sample.

The presence of acicular ferrite with the sawteeth shape under the conditions of higher current (i.e., Fig. 5(b) and Fig. 6(b)) suggests, according to Cheng et al. (2010), the formation of primary Widmanstätten ferrite which has started to nucleate at the ferrite grain boundaries. These morphology changes in the ferrite lead to grain size reductions compared to HAZ even when the FZ is the most thermally affected areas. Therefore, it can be inferred that higher voltages and currents do not negatively affect the welded joint properties.

Fig. 7 allows visualizing that the FZ and the HAZ occupy a greater area as the current and voltage of the welding process increases. The length of each welding zone was assessed as the average distance between the beginning and end of each zone in the normal direction (ND). In this way, welding processes under the conditions of 125A-10V and 150A-10V have a greater impact on the base material microstructure, as well as on its mechanical response. Thakur and Chapgaon (2016) highlighted that wider HAZs generated by higher heat input due to increased current produce more significant hardness changes due to the formation of larger grain sizes.
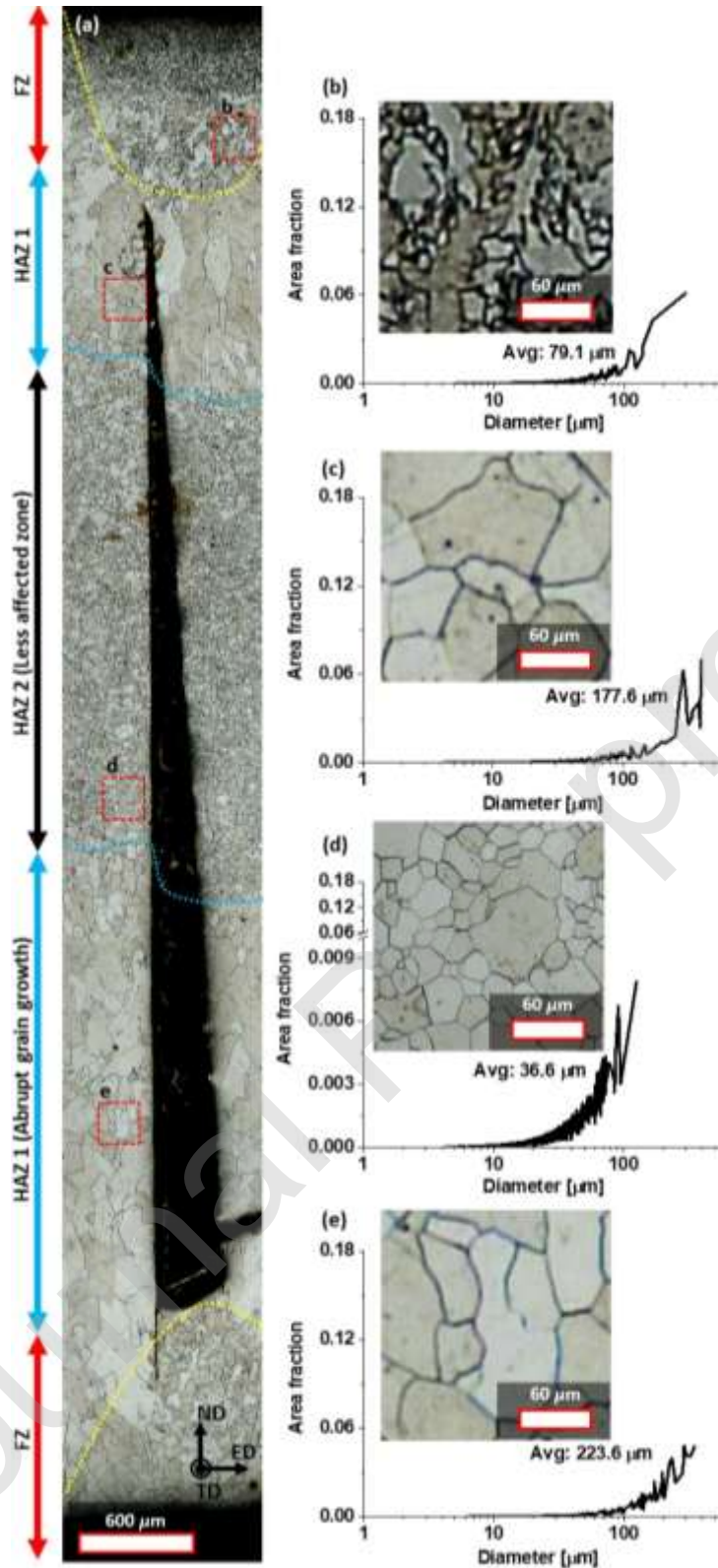
Fig. 6. Microstructure evolution for the 150A-10V-45s condition across the sample diameter, (a) microstructure evolution indicating the different zones after the welding process, (b) grain size values around the FZ, (c) grain size values around the HAZ 1, (d) grain size values around the HAZ 2, and (e) grain size values around the HAZ 1 (the amplified areas for figures 6(b), 6(c), 6(d), and 6(e) correspond with the red dash squares tagged with letters b, c, d, and e, respectively).

13

Fig. 4-7 demonstrate that the weld around the perimeter of the bars affected the entire microstructure along the diameter of the samples. Based on the grain sizes obtained in each zone, it is clear that recrystallization has taken place across the diameter of the piece, removing the nanostructured microstructure of the BM. In this way, the microstructure in the HAZ 1 is associated with recrystallization and subsequent abnormal grain growth phenomena, while the new grains in HAZ 2 are due to the static recrystallization occurrence.
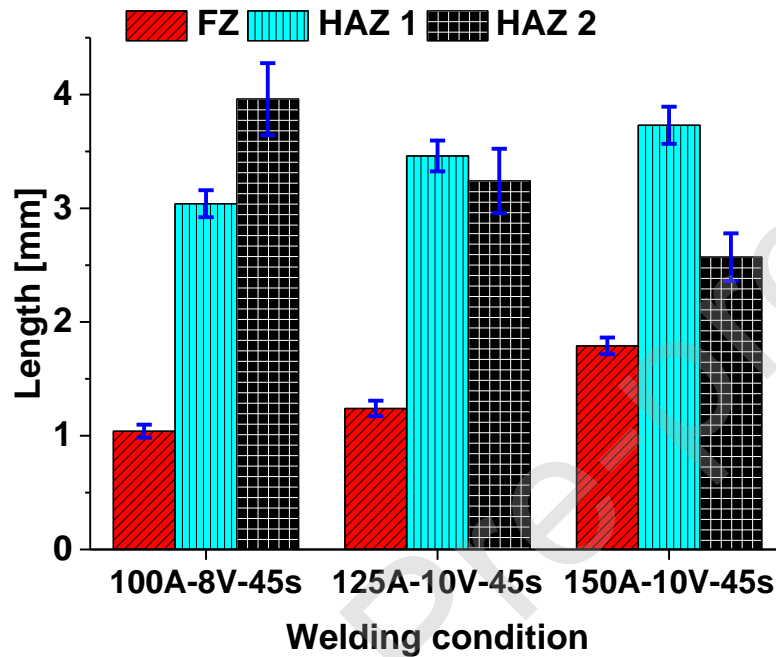

Fig. 7. FZ, HAZ 1, and HAZ 2 sizes for the three welding conditions.

Fig. 8 plots the grain size and hardness evolution across the welded bars diameter where one can notice the manifested material heterogeneity. Fig. 8(a) shows that for the welding conditions with higher current, there are more substantial grain size changes as a consequence of the HAZ 1 broadening and the HAZ 2 narrowing. These microstructural changes are attributed to the temperature gradients generated by the welding process. García-García et al. (2019) demonstrated that GTAW involves temperatures above 1000 °C. These temperatures are higher than the Armco iron recrystallization temperature after 8 ECAP passes, which is between 450 °C and 570 °C according to Muñoz et al. (2018) previous studies by differential scanning calorimetry using different heating rates. Additionally, Fig. 8(a) confirms that around the bars perimeters (FZ neighborhoods), there is a grain size similar to that of the HAZ 2, while the largest grain growths are in the HAZ 1. Thus, it is confirmed that the GTAW process

14

introduced temperatures of at least 450 °C on the BM since the grain size grew in all areas with respect to the initial ultrafine state.

Regarding the hardness evolution, Fig. 8(b) shows an overall hardness decrease around the welded joint for the three welding conditions analyzed in this study compared with the ultrafine grain material (8 ECAP passes), but still maintains higher values than the initial annealed material. It is worth noting that the hardness measurements close to the FZ are slightly higher than in the other zones, especially in the 150A-10V-45s condition where the nucleation of acicular ferrite (also known as Widmanstätten ferrite) around the grain boundaries is observed, as shown in Fig. 6(b). Lin et al. (2018) demonstrated that this phase usually forms at temperatures around A_{e3} and may play an essential role in the hardening of steels.
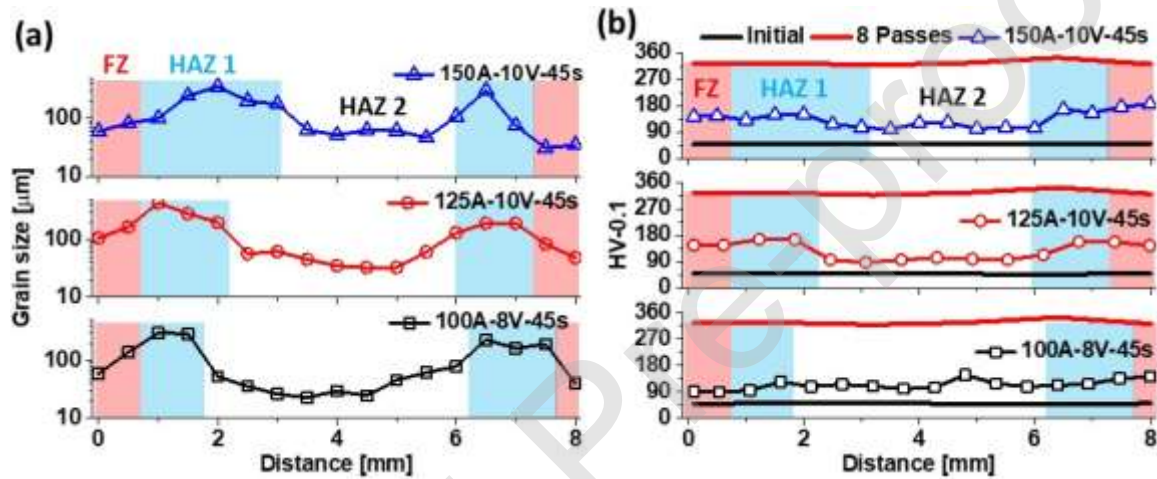

Fig. 8. (a) Grain size profiles across the sample diameter, and (b) hardness evolution across the sample diameter for the three GTAW conditions.

The possible causes that the hardness evolution shows lower values in HAZ 2, which has a smaller grain size than HAZ 1, where there was an evident abnormal grain growth, can be attributed to the high residual stresses and the heterogeneous grain size produced by the temperature gradients of the GTAW process. Several authors like Lai and Wu, (2020) have indicated that higher residual tensile stresses are introduced in the vicinity of the FZ than in the vicinity of the BM when linear weld joints are made in sheets. On the other hand, Wu and Kim (2018) concluded that in welds on cylindrical elements such as pipes, the distribution of residual stresses follows a mixed behavior between tensile residual stresses inside the tube and compression components in its outside. For example, after subjecting an austenitic stainless steel tube to GTAW welding, Ravisankar et al. (2014) indicated a transition from tensile residual stresses to compression state around 1.5 mm from the outside in the radial direction.

15

3.3 Thermal stability

In order to analyze in more detail the different microstructural changes observed throughout the welded joint and to understand their effects on mechanical properties, heat treatments were performed using high heating and cooling rates in the austenitic region to try to simulate temperatures reached during the welding process. The thermal cycles were performed using two maximum temperatures, one temperature slightly higher than A_{e3} (950 °C) and a second temperature much higher than A_{e3} (1150 °C). Fig. 9(a) indicates the thermal cycles carried out in a quenching dilatometry under a protective argon atmosphere. Further, Fig. 9(b) shows the dilatometry curves highlighting the more prominent material expansion at 1150 °C than 950 °C as a result of the phase transformation from ferrite to austenite.
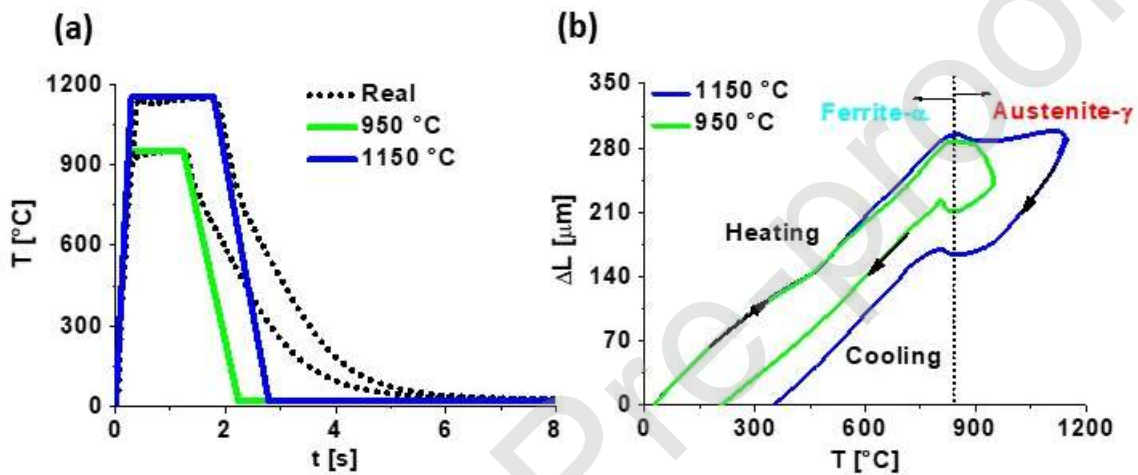

Fig. 9. (a) Thermal cycles for the 950 ℃ and 1150 ℃ heat treatments, and (b) dilatometry curves for the two heat treatments.

After performing the heat treatments, Fig. 10 indicates the microstructures obtained in each case, as well as their main microstructural characteristics such as grain size and the GNDs distribution. After the heat treatment at 950 °C, Fig. 10(a) presents a new microstructure with an evident grain growth with a polygonal morphology (straight grain boundaries). On the other hand, in Fig. 10(b), after heating up to 1150 °C, the microstructure presents an unusual morphology with an entirely different acicular shape than those obtained in the initial material or after deformation by ECAP. This type of morphology is very similar to that obtained in the FZ of the welding condition 150A-10V-45s, which is Widmanstätten ferrite.

As a consequence of the high temperatures generated in the FZ, different types of phase transformation can occur during the subsequent cooling depending on the number of alloying elements contained in the steel. For example, Arivazhagan et al. (2011) demonstrated that the welded joint hardness decreases as the ferrite (δ) content increases, while Madhavan et al.

16

(2020) welded a high chromium steel with enhanced mechanical properties due to finer weld microstructures. However, Armco iron is almost pure iron, with no amount of alloying elements, which means that it does not present many possible variations in phase transformations. Several authors have reported the formation of Widmanstätten ferrite in temperature ranges above A_{e3}. Grewal et al. (2016) obtained Widmanstätten ferrite under conditions of compression deformation in the austenitic range, and Cheng et al. (2010) employed heat treatments at several temperatures inside the austenite region in low carbon steel to study the different Widmanstätten ferrite morphologies through three-dimensional reconstruction techniques..

The appearance of the different ferrite morphologies generated microstructural changes that mainly affected the grain size and the nature of the grain boundaries. Fig. 10(c) illustrates the grain size evolution for the two heat treatment conditions, demonstrating intermediate behaviors between the initial material and the 8 ECAP passes condition. The mean grain size values were 8.73 µm and 1.88 µm for the 950 °C and 1150 °C treatments, respectively. Of course, these grains are not in the same order than in the 8 ECAP pass samples, but they are still significantly low, especially the size attained after heating at 1150 ºC, achieving even the ultrafine grain size regime

It is worth mentioning that after subjecting the material to these temperatures (950 °C and 1150 °C) the two conditions continue showing high densities of GNDs (Fig. 10(d)) compared to the initial material with average values around 8×10^{13} m^{-2} and 1×10^{14} m^{-2}. However, Fig. 10(a)-10(b) illustrate through the GND maps that its distribution is more homogeneous than in the initial and 8 ECAP passes materials (Fig. 2(a)-2(b)), where certain regions formed high-density GND walls. This behavior explains that, although the material was heated at temperatures higher than its recrystallization temperature, it still retains a microstructure with high GND densities (higher internal energy) that allows keeping small grain sizes and hence superior strength than the initial condition.
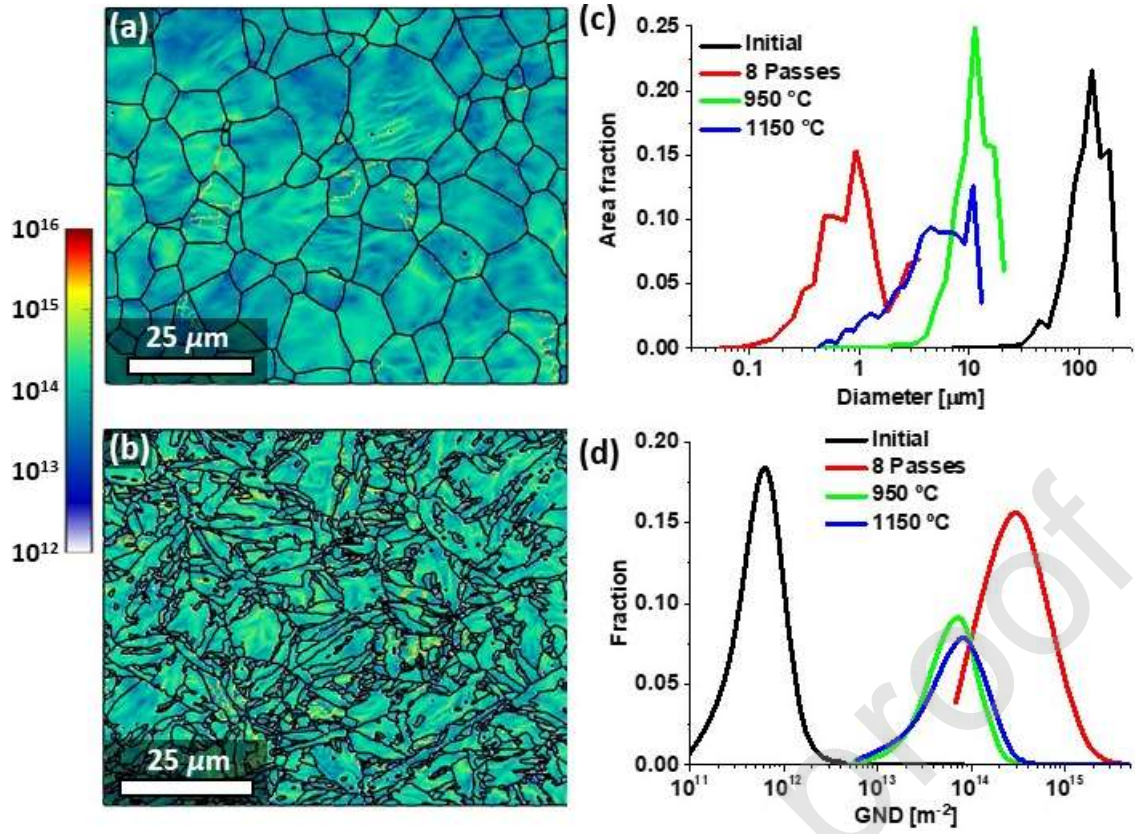
Fig. 10. GND maps after the heat treatments, (a) 950 ℃, (b) 1150 ℃, (c) grain size evolution after the heat treatments, and (d) GND distributions.

The grain boundaries energy associated with the GNDs can be assessed with the Read-Shockley equation (Humphreys and Hatherly, 2004):

$$\gamma(\theta) = \begin{cases} \gamma_m \; if \; \theta > \theta_m \\ \gamma_m \left(\dfrac{\theta}{\theta_m}\right)\left[1 - ln\left(\dfrac{\theta}{\theta_m}\right)\right] \; if \; \theta < \theta_m \end{cases} \tag{1}$$

where $\gamma_m = 0.617 \; Jm^{-2}$ is the energy per unit area of a High Angle Grain Boundary (HAGB), θ represents the different values of misorientation, and $\theta_m = 15°$ is the misorientation threshold above which the energy per unit area is not dependent on the misorientation angle. The mean energy can be obtained using the following summation (Hazra et al., 2009):

$$\bar{\gamma} = \sum_{2}^{62.8} [\gamma(\theta)f(\theta)] \tag{2}$$

18

where *f(θ)* accounts for the grain boundaries fraction for an appropriate misorientation, according to Rohrer (2011), the stored energy in the grain boundaries (E_b) can be approximated following the next equation:

$$E_b = S_V \bar{\gamma} = \frac{2\bar{\gamma}}{d_{sub}} \tag{3}$$

where, S_V is the area per unit volume ($S_V \sim 2/d_{sub}$), and d_{sub} is the subgrain size.

Using Eq. (1)-(3) and the grain sizes summarized in Table 2, the energy stored at the grain boundaries can be calculated. At first glance, Table 2 demonstrates the energy stored at the boundaries increases abruptly after ECAP processing, going from 0.1 J/mol to 24.9 J/mol. After the heat treatments at 950 °C and 1150 °C, the energy at the boundaries decreases although it is still higher than in the initial condition with values of 1 J/mol and 4.4 J/mol, respectively. This behavior demonstrates that the temperature range between 950 °C and 1150 °C affects the ultrafine microstructure. However, it still maintains some ultrafine grain microstructural characteristics (e.g., grain size and GND) as long as fast heating and cooling rates are employed.

These higher energies after heat treatments concerning the initial material are due to the smaller sub-grain size, as evidenced by the high dislocation density associated with Low Angle Grain Boundary (LAGB) in Table 2. According to Hughes and Hansen (2000) single-phase materials strength such as Armco iron can be analyzed, taking into account the subgrains and grains contributions following Eq. (4)-(5).

$$\sigma_{SGB} = \alpha \mu M b \sqrt{\rho_{LAGB}} \tag{4}$$

$$\sigma_{GB} = k \left(\frac{f_{HAGB}}{d} \right)^{1/2} \tag{5}$$

with $\rho_{LAGB} = \frac{3(f_{LAGB})\bar{\theta}_{LAGB}}{b \cdot d_{sub}}$, where $\bar{\theta}_{LAGB}$ represents the average misorientation of the LAGB, f_{LAGB} the low angle grain boundaries fraction, M the Taylor factor (3.02 for Armco iron), d the grain size, k the Hall-Petch constant (0.36 MPa m$^{1/2}$ for Armco iron), f_{HAGB} the high angle grain boundaries fraction, μ the shear module (80 GPa for Armco iron), and α a constant equal to 0.3 obtained from the research work of Muñoz et al. (2017a) for Armco iron processed by ECAP

19

at different strain magnitudes. In this way, it can be corroborated by the values recorded in Table 2 that the subgrains strength contribution is significant, reaching, e.g., almost 50% of the global strength of the nanostructured material. It is also confirmed that the Widmanstätten type microstructures show higher strength contributions than those of equiaxed grains due not only to the large subgrains fraction but also to the smaller grain sizes achieved by their morphology.

Table 2. Microstructure properties

Condition	Subgrain size [μm]	Grain size [μm]	f_{LAGB}	ρ_{LAGB} [m^{-2}]	$\overline{\gamma}$ [J/m^2]	E_b [J/mol]	σ_{SGB} [MPa]	σ_{GB} [MPa]
Initial	71.3	90.1	0.05	8.53×10^{10}	0.59	0.1	19.2	37
8 Passes	0.3	0.5	0.41	4.25×10^{14}	0.54	24.9	308.3	404.8
950 °C	7.6	8.7	0.36	1.02×10^{13}	0.54	1.0	61.8	97.7
1150 °C	1.6	1.9	0.52	1.26×10^{14}	0.49	4.4	207.4	181.5

The EBSD and LOM microstructural evolution demonstrates the possible formation of decreasing LAGB fraction and dislocation gradients from the outside to the inside of the bar in the radial direction. This behavior, together with the possible higher residual stresses in the vicinity of HAZ 1, helps to explain the higher hardness values in this area than in HAZ 2. Finally, it can be established that during the GTAW welding process, the ultrafine grain Armco iron can still retain superior mechanical and microstructural properties than the initial material condition besides losing the original nanostructured grains. However, the dilatometric results indicate a large potential to retain the microstructure, suggesting that alternative welding process (with lower heat input) should be studied to retain as much as possible the ultrafine microstructure.

4   Conclusions

After processing Armco iron through severe plastic deformation by ECAP up to 8 passes and welding it using the GTAW process, the following conclusions summarize the main findings of this research work:

1) The ECAP process generated an ultra-fine grain size material with high dislocation density and grain boundaries energies resulting in a strength four times higher than the initial material.

2) The different welding conditions used generated different zones (i.e., FZ, HAZ 1, and HAZ 2) with different grain sizes and morphologies over the welded joint and surrounding areas as a consequence of temperature variations across the welded pieces diameter.

3) The welding conditions that involved higher current and voltage (i.e., higher heat input) not only generate larger FZ and HAZ, leading to larger grain sizes but also a different acicular ferrite morphology in the FZ (i.e., Widmanstätten ferrite).

4) The formation of Widmanstätten ferrite was also confirmed by dilatometry and EBSD tests. This microstructure generated smaller grain size in the FZ, giving rise to higher hardness.

5) Armco iron processed by ECAP and subsequently welded by the GTAW process reduced its mechanical properties compared to the material with 8 ECAP passes, but still maintained better properties than the initial material due to the promotion of a relatively fine recrystallized grains (HAZ 2) and the presence of HAZ 1 formed by high dislocation densities and grain boundary energies associated to Widmanstätten ferrite.

6) The dilatometric tests suggest high potential to retain fine microstructures if low heat inputs welding techniques are used

Credit authorship contribution statement

Jairo Alberto Muñoz: Investigation, formal analysis, writing original draft, writing review and editing **Alexander Komissarov:** Supervision, funding acquisition, investigation. **Ignacio Mejía:** Supervision, formal analysis, methodology. **Humberto Hernández-Belmontes:** Investigation, methodology, data acquisition. **José María Cabrera:** Supervision, writing review and editing, resources, project administration, funding acquisition, data curation.

Declaration of interests

The authors declare that they have no known competing financial interests or personal relationships that could have appeared to influence the work reported in this paper.

Acknowledgements

Interest conflict: None

References

Arivazhagan, B., Srinivasan, G., Albert, S.K., Bhaduri, A.K., 2011. A study on influence of heat input variation on microstructure of reduced activation ferritic martensitic steel weld metal produced by GTAW process. Fusion Eng. Des. 86, 192–197. https://doi.org/https://doi.org/10.1016/j.fusengdes.2010.12.035

Bachmann, F., Hielscher, R., Schaeben, H., 2010. Texture Analysis with MTEX – Free and Open Source Software Toolbox. Solid State Phenom. 160, 63–68. https://doi.org/10.4028/www.scientific.net/SSP.160.63

Bagherpour, E., Pardis, N., Reihanian, M., Ebrahimi, R., 2019. An overview on severe plastic deformation: research status, techniques classification, microstructure evolution, and applications. Int. J. Adv. Manuf. Technol. 100, 1647–1694. https://doi.org/10.1007/s00170-018-2652-z

Beyerlein, I.J., Tóth, L.S., 2009. Texture evolution in equal-channel angular extrusion. Prog. Mater. Sci. 54, 427–510. https://doi.org/https://doi.org/10.1016/j.pmatsci.2009.01.001

Cheng, L., Wan, X.L., Wu, K.M., 2010. Three-dimensional morphology of grain boundary Widmanstätten ferrite in a low carbon low alloy steel. Mater. Charact. 61, 192–197. https://doi.org/https://doi.org/10.1016/j.matchar.2009.11.009

García-García, V., Mejía, I., Reyes-Calderón, F., 2019. Quantitative metallographic characterization of welding microstructures in Ti-containing TWIP steel by means of image processing analysis. Mater. Charact. 147, 1–10. https://doi.org/10.1016/j.matchar.2018.10.012

Gharibshahiyan, E., Raouf, A.H., Parvin, N., Rahimian, M., 2011. The effect of microstructure on hardness and toughness of low carbon welded steel using inert gas welding. Mater. Des. 32, 2042–2048.

https://doi.org/https://doi.org/10.1016/j.matdes.2010.11.056

Grewal, R., Aranas, C., Chadha, K., Shahriari, D., Jahazi, M., Jonas, J.J., 2016. Formation of Widmanstätten ferrite at very high temperatures in the austenite phase field. Acta Mater. 109, 23–31. https://doi.org/https://doi.org/10.1016/j.actamat.2016.02.062

Hazra, S.S., Gazder, A.A., Pereloma, E. V, 2009. Stored energy of a severely deformed interstitial free steel. Mater. Sci. Eng. A 524, 158–167. https://doi.org/https://doi.org/10.1016/j.msea.2009.06.033

Huang, Y., Langdon, T.G., 2013. Advances in ultrafine-grained materials. Mater. Today 16, 85–93. https://doi.org/https://doi.org/10.1016/j.mattod.2013.03.004

Hughes, D.A., Hansen, N., 2000. Microstructure and strength of nickel at large strains. Acta Mater. 48, 2985–3004. https://doi.org/https://doi.org/10.1016/S1359-6454(00)00082-3

Humphreys, F.J., Hatherly, M., 2004. Chapter 4 - The Structure and Energy of Grain Boundaries, in: Humphreys, F.J., Hatherly, M. (Eds.), Recrystallization and Related Annealing Phenomena (Second Edition). Elsevier, Oxford, pp. 91–119. https://doi.org/https://doi.org/10.1016/B978-008044164-1/50008-6

Igathinathane, C., Pordesimo, L.O., Columbus, E.P., Batchelor, W.D., Methuku, S.R., 2008. Shape identification and particles size distribution from basic shape parameters using ImageJ. Comput. Electron. Agric. 63, 168–182. https://doi.org/10.1016/j.compag.2008.02.007

Ko, Y.G., Hamad, K., 2018. Analyzing the thermal stability of an ultrafine grained interstitial free steel fabricated by differential speed rolling. Mater. Sci. Eng. A 726, 32–36. https://doi.org/https://doi.org/10.1016/j.msea.2018.04.068

Lai, H.-H., Wu, W., 2020. Practical examination of the welding residual stress in view of low-carbon steel welds. J. Mater. Res. Technol. https://doi.org/https://doi.org/10.1016/j.jmrt.2020.01.004

Lathabai, S., 2011. 20 - Joining of aluminium and its alloys, in: Lumley, R. (Ed.), Fundamentals of Aluminium Metallurgy, Woodhead Publishing Series in Metals and Surface Engineering. Woodhead Publishing, pp. 607–654. https://doi.org/https://doi.org/10.1533/9780857090256.3.607

Lin, C., Wan, J., Ruan, H., 2018. Phase field modeling of Widmanstätten ferrite formation in steel. J. Alloys Compd. 769, 620–630. https://doi.org/https://doi.org/10.1016/j.jallcom.2018.07.372

Madhavan, S., Kamaraj, M., Arivazhagan, B., 2020. A comparative study on the microstructure and mechanical properties of fusion welded 9 Cr-1 Mo steel. J. Mater. Res. Technol. 9, 2223–2229. https://doi.org/https://doi.org/10.1016/j.jmrt.2019.12.053

Messler Jr, R.W., 1999. Principles of Welding; Processes, Physics, Chemistry, and Metallurgy, John Willey & Sons, Inc., New York. New York.

Muñoz, J.A., 2019. Geometrically Necessary Dislocations (GNDs) in iron processed by Equal Channel Angular Pressing (ECAP). Mater. Lett. 238, 42–45. https://doi.org/https://doi.org/10.1016/j.matlet.2018.11.142

Muñoz, J.A., Higuera, O.F., Benito, J.A., Bradai, D., Khelfa, T., Bolmaro, R.E., Jorge, A.M., Cabrera, J.M., 2019. Analysis of the micro and substructural evolution during severe plastic deformation of ARMCO iron and consequences in mechanical properties. Mater. Sci. Eng. A 740–741, 108–120. https://doi.org/https://doi.org/10.1016/j.msea.2018.10.100

Muñoz, J.A., Higuera, O.F., Cabrera, J.M., 2017a. High cycle fatigue of ARMCO iron severely deformed by ECAP. Mater. Sci. Eng. A 681, 85–96. https://doi.org/https://doi.org/10.1016/j.msea.2016.10.010

Muñoz, J.A., Higuera, O.F., Cabrera, J.M., 2017b. Microstructural and mechanical study in the plastic zone of ARMCO iron processed by ECAP. Mater. Sci. Eng. A 697, 24–36. https://doi.org/10.1016/j.msea.2017.04.108

Muñoz, J.A., Higuera, O.F., Expósito, A.H., Boulaajaj, A., Bolmaro, R.E., Dumitru, F.D., Calvillo, P.R., Jorge, A.M., Cabrera, J.M., 2018. Thermal stability of ARMCO iron processed by ECAP. Int. J. Adv. Manuf. Technol. 98, 2917–2932. https://doi.org/10.1007/s00170-018-2353-7

Murugan, S., Rai, S.K., Kumar, P. V, Jayakumar, T., Raj, B., Bose, M.S.C., 2001. Temperature distribution and residual stresses due to multipass welding in type 304 stainless steel and low carbon steel weld pads. Int. J. Press. Vessel. Pip. 78, 307–317. https://doi.org/https://doi.org/10.1016/S0308-0161(01)00047-3

Owunna, I., Ikpe, A., Achebo, J.I., 2018. 3D Finite Element Modelling of Weld Bead
Penetration in Tungsten Inert Gas (TIG) Welding of AISI 1020 Low Carbon Steel Plate.
Eur. Mech. Sci. 2, 96–105. https://doi.org/10.26701/ems.441446

Ravisankar, A., Velaga, S.K., Rajput, G., Venugopal, S., 2014. Influence of welding speed
and power on residual stress during gas tungsten arc welding (GTAW) of thin sections
with constant heat input: A study using numerical simulation and experimental
validation. J. Manuf. Process. 16, 200–211. https://doi.org/10.1016/j.jmapro.2013.11.002

Rohrer, G.S., 2011. Grain boundary energy anisotropy: a review. J. Mater. Sci. 46, 5881–
5895. https://doi.org/10.1007/s10853-011-5677-3

Singh, G., Saxena, R.K., Pandey, S., 2020. An examination of mechanical properties of
dissimilar AISI 304 stainless steel and copper weldment obtained using GTAW. Mater.
Today Proc. https://doi.org/https://doi.org/10.1016/j.matpr.2020.02.579

Thakur, P.P., Chapgaon, A.N., 2016. A Review on Effects of GTAW Process Parameters on
weld. Int. J. Res. Appl. Sci. Eng. Technol. 4, 136–140.
https://doi.org/10.13140/RG.2.2.11535.38569

Valiev, R.Z., Enikeev, N.A., Murashkin, M.Y., Kazykhanov, V.U., Sauvage, X., 2010. On the
origin of the extremely high strength of ultrafine-grained Al alloys produced by severe
plastic deformation. Scr. Mater. 63, 949–952.
https://doi.org/https://doi.org/10.1016/j.scriptamat.2010.07.014

Wang, H., Hu, S., Shen, J., Li, D., Lu, J., 2017. Effect of duty cycle on microstructure and
mechanical properties of pulsed GTAW lap joint of Invar. J. Mater. Process. Technol.
243, 481–488. https://doi.org/10.1016/j.jmatprotec.2017.01.008

Wu, C., Kim, J.W., 2018. Analysis of welding residual stress formation behavior during
circumferential TIG welding of a pipe. Thin-Walled Struct. 132, 421–430.
https://doi.org/10.1016/j.tws.2018.09.020

Yang, Y., Yan, B., Li, J., Wang, J., 2011. The effect of large heat input on the microstructure
and corrosion behaviour of simulated heat affected zone in 2205 duplex stainless steel.
Corros. Sci. 53, 3756–3763. https://doi.org/10.1016/j.corsci.2011.07.022

Yoda, R., Shibata, K., Morimitsu, T., Terada, D., Tsuji, N., 2011. Formability of ultrafine-

grained interstitial-free steel fabricated by accumulative roll-bonding and subsequent annealing. Scr. Mater. 65, 175–178. https://doi.org/https://doi.org/10.1016/j.scriptamat.2011.02.002

Yousefieh, M., Shamanian, M., Saatchi, A., 2011. Influence of Heat Input in Pulsed Current GTAW Process on Microstructure and Corrosion Resistance of Duplex Stainless Steel Welds. J. Iron Steel Res. Int. 18, 65–69. https://doi.org/10.1016/S1006-706X(12)60036-3

Figure captions

Figure 1. (a) ECAP die set up, and (b) welding process description for the 8 ECAP passes material.
Figure 2. Materials characterization a) EBSD map (GND and IPF) and (110) pole figure for the initial annealed material, b) EBSD map (GND and IPF) and (110) pole figure for the 8 ECAP passes material, c) grain size comparison, d) misorientation angle evolution of each condition, e) tensile properties for both the initial and 8 ECAP passes materials.
Figure 3. Welded butt joints of the 8 ECAP passes sample at different conditions, a) 100A-8V-45s, b) 125A-10V-45s, and c) 150A-10V-45s.
Figure 4. Microstructure evolution for the 100A-8V-45s condition across the sample diameter, (a) microstructure evolution indicating the different zones after the welding process, (b) grain size values around the FZ, (c) grain size values around the HAZ 1, (d) grain size values around the HAZ 2, and (e) grain size values around the HAZ 1 (the amplified areas for figures 4(b), 4(c), 4(d), and 4(e) correspond with the red dash squares tagged with letters b, c, d, and e, respectively).
Figure 5. Microstructure evolution for the 125A-10V-45s condition across the sample diameter, (a) microstructure evolution indicating the different zones after the welding process, (b) grain size values around the FZ, (c) grain size values around the HAZ 1, (d) grain size values around the HAZ 2, and (e) grain size values around the HAZ 1 (the amplified areas for figures 5(b), 5(c), 5(d), and 5(e) correspond with the red dash squares tagged with letters b, c, d, and e, respectively).
Figure 6. Microstructure evolution for the 150A-10V-45s condition across the sample diameter, (a) microstructure evolution indicating the different zones after the welding process, (b) grain size values around the FZ, (c) grain size values around the HAZ 1, (d) grain size values around the HAZ 2, and (e) grain size values around the HAZ 1 (the amplified areas for figures 6(b), 6(c), 6(d), and 6(e) correspond with the red dash squares tagged with letters b, c, d, and e, respectively).
Figure 7. FZ, HAZ 1, and HAZ 2 sizes for the three welding conditions.
Figure 8. a) Grain size profiles across the sample diameter, and b) hardness evolution across the sample diameter for the three GTAW conditions.
Figure 9. Thermal cycles for the 950 ºC and 1150 ºC heat treatments, and b) dilatometry curves for the two heat treatments.
Figure 10. GND maps after the heat treatments, a) 950 ºC, b) 1150 ºC, c) grain size evolution after the heat treatments, and d) GND distributions.

Table captions

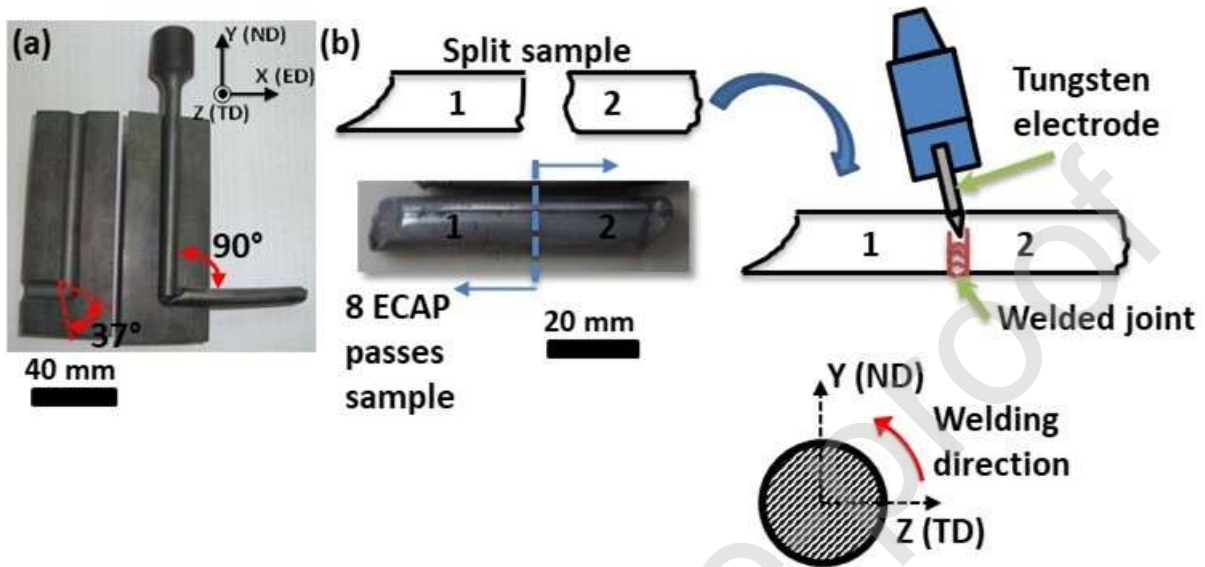Table 1. Chemical composition of Armco iron.
Table 2. Microstructure properties

Figure 1. (a) ECAP die set up, and (b) welding process description for the 8 ECAP passes material.
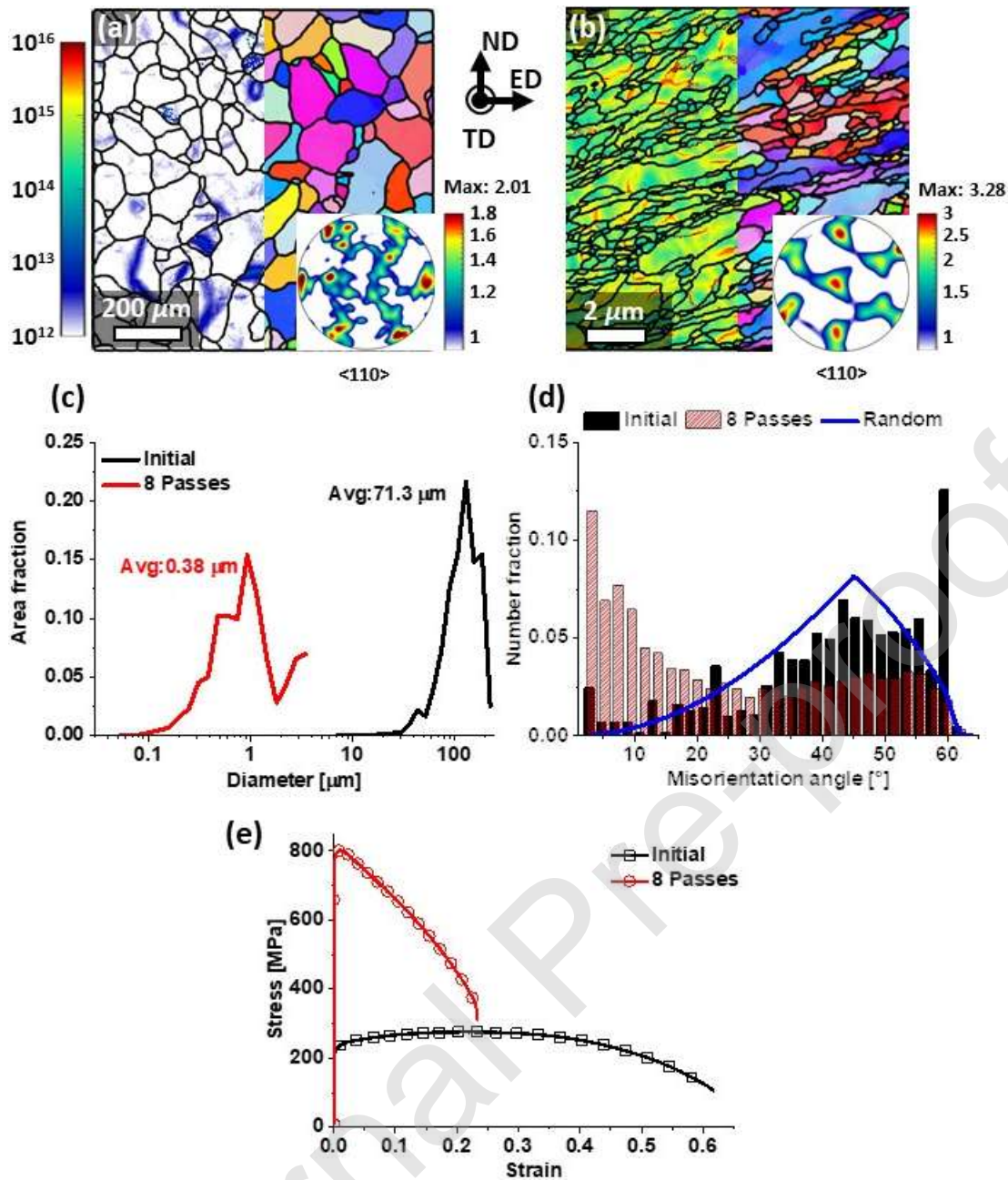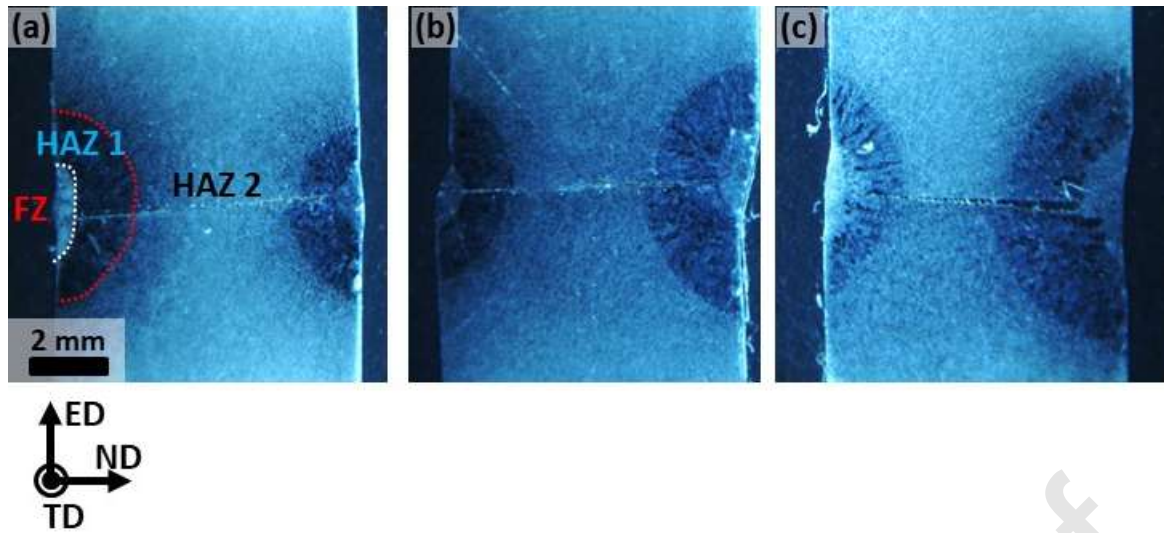
Figure 2. Materials characterization a) EBSD map (GND and IPF) and (110) pole figure for the initial annealed material, b) EBSD map (GND and IPF) and (110) pole figure for the 8 ECAP passes material, c) grain size comparison, d) misorientation angle evolution of each condition, e) tensile properties for both the initial and 8 ECAP passes materials.

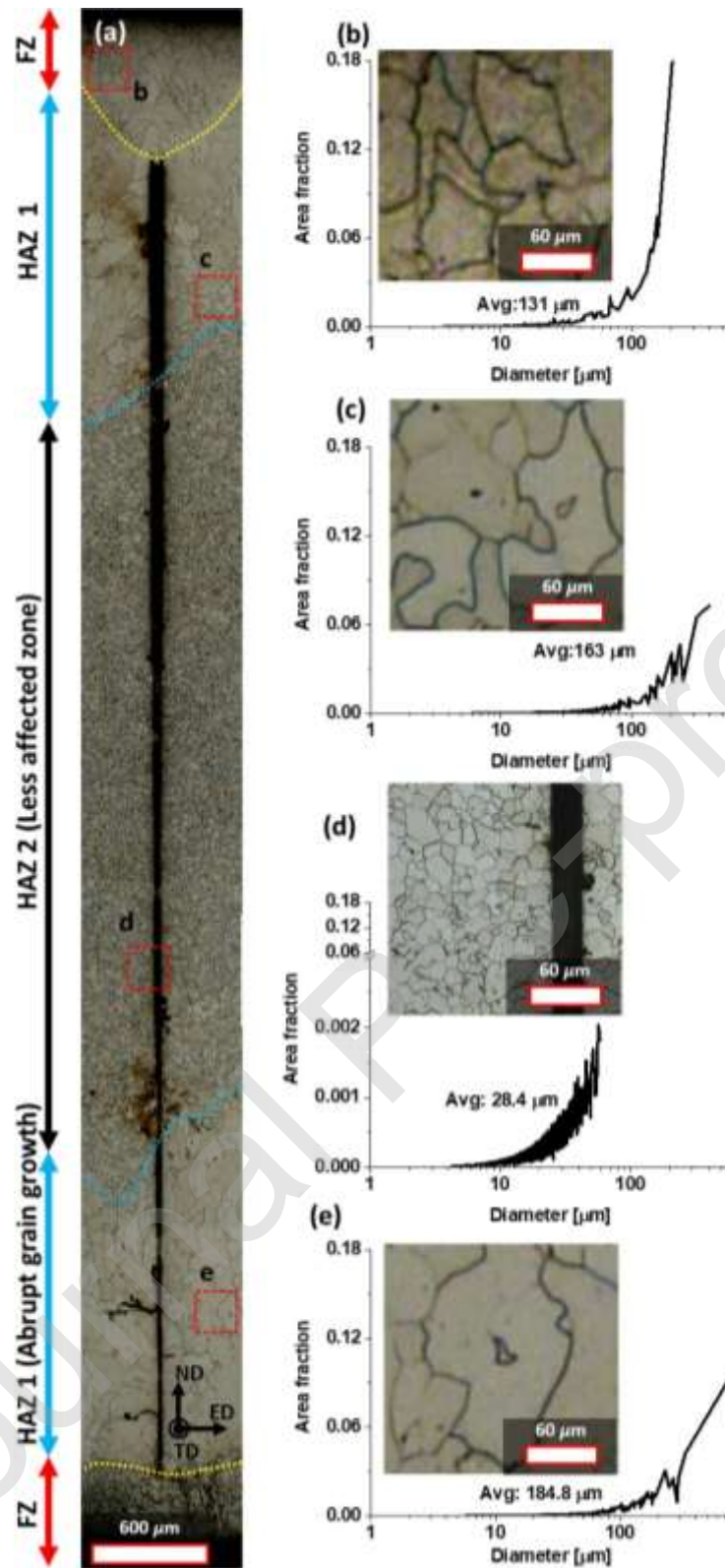**Figure 3.** Welded butt joints of the 8 ECAP passes sample at different conditions, a) 100A-8V-45s, b) 125A-10V-45s, and c) 150A-10V-45s.

Figure 4. Microstructure evolution for the 100A-8V-45s condition across the sample diameter, (a) microstructure evolution indicating the different zones after the welding process, (b) grain size values around the FZ, (c) grain size values around the HAZ 1, (d) grain size values around the HAZ 2, and (e) grain size values around the HAZ 1 (the amplified areas for figures 4(b), 4(c), 4(d), and 4(e) correspond with the red dash squares tagged with letters b, c, d, and e, respectively).
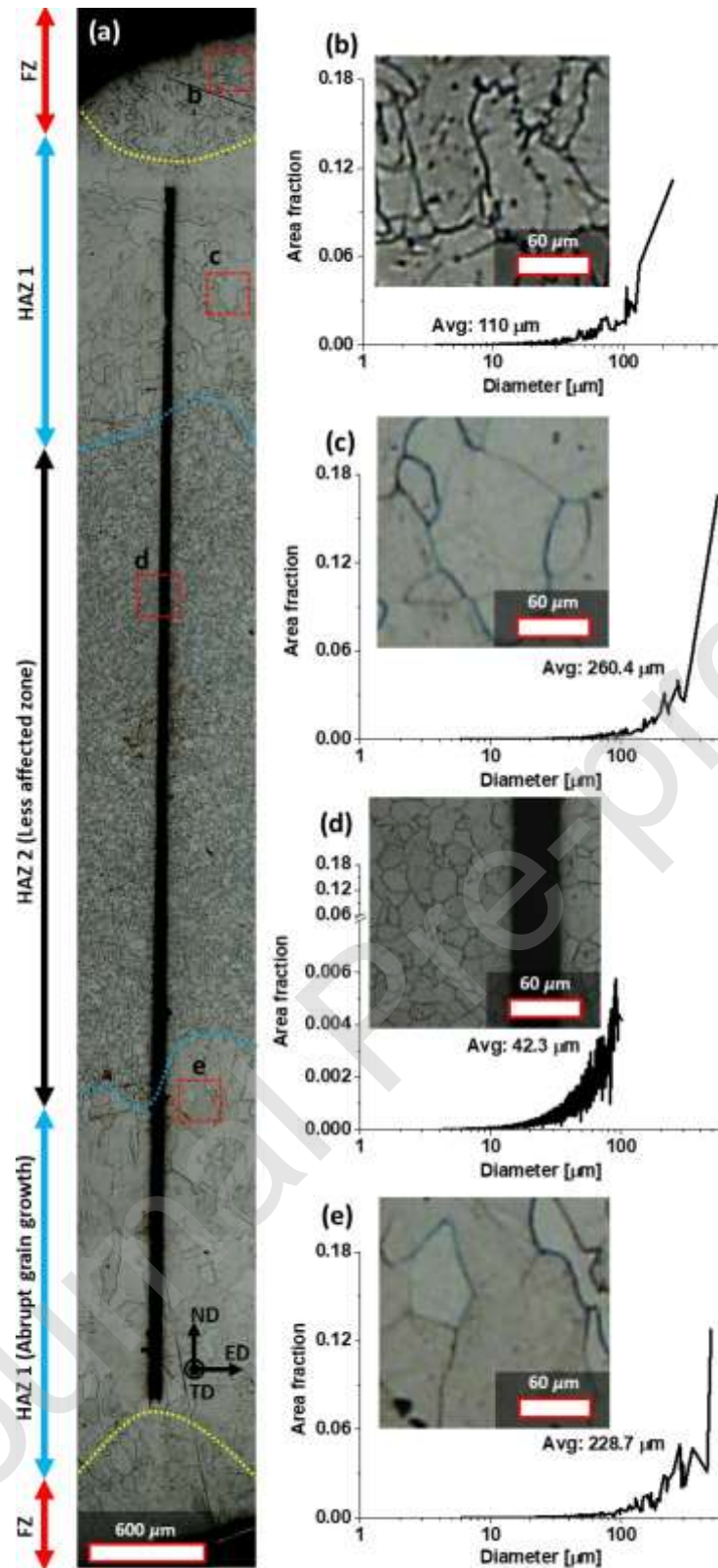
Figure 5. Microstructure evolution for the 125A-10V-45s condition across the sample diameter, (a) microstructure evolution indicating the different zones after the welding process, (b) grain size values around the FZ, (c) grain size values around the HAZ 1, (d) grain size values around the HAZ 2, and (e) grain size values around the HAZ 1 (the amplified areas for figures 5(b), 5(c), 5(d), and 5(e) correspond with the red dash squares tagged with letters b, c, d, and e, respectively).
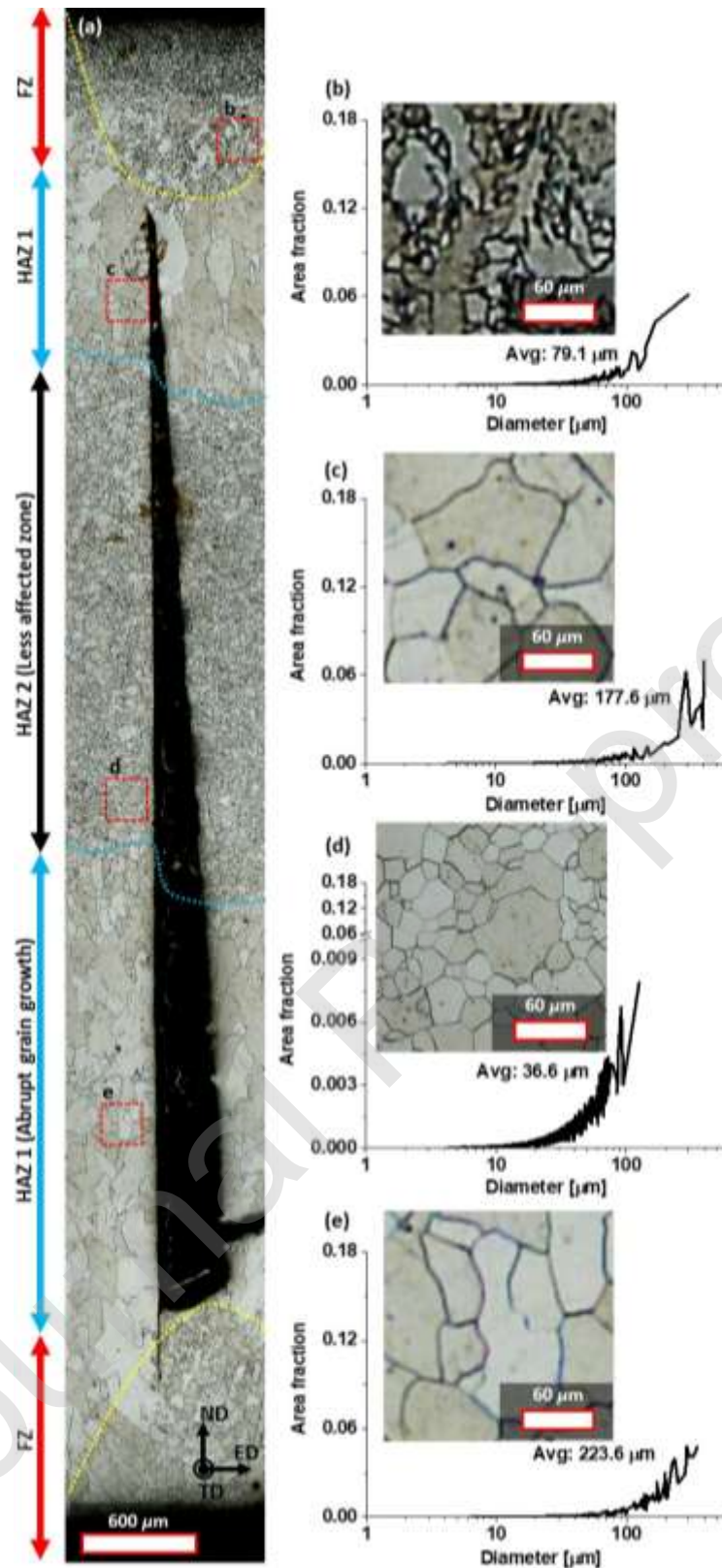
31

Figure 6. Microstructure evolution for the 150A-10V-45s condition across the sample diameter, (a) microstructure evolution indicating the different zones after the welding process, (b) grain size values around the FZ, (c) grain size values around the HAZ 1, (d) grain size values around the HAZ 2, and (e) grain size values around the HAZ 1 (the amplified areas for figures 6(b), 6(c), 6(d), and 6(e) correspond with the red dash squares tagged with letters b, c, d, and e, respectively).
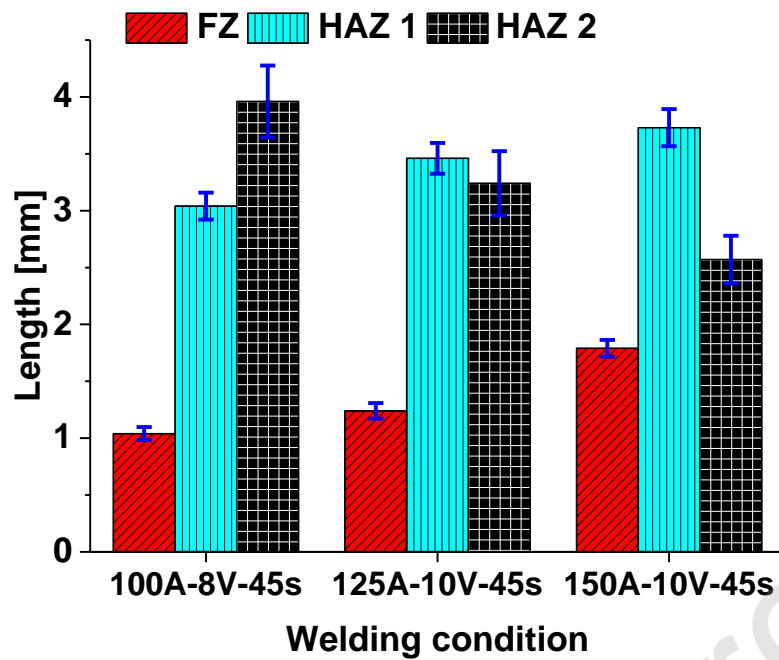
32

Figure 7. FZ, HAZ 1, and HAZ 2 sizes for the three welding conditions.

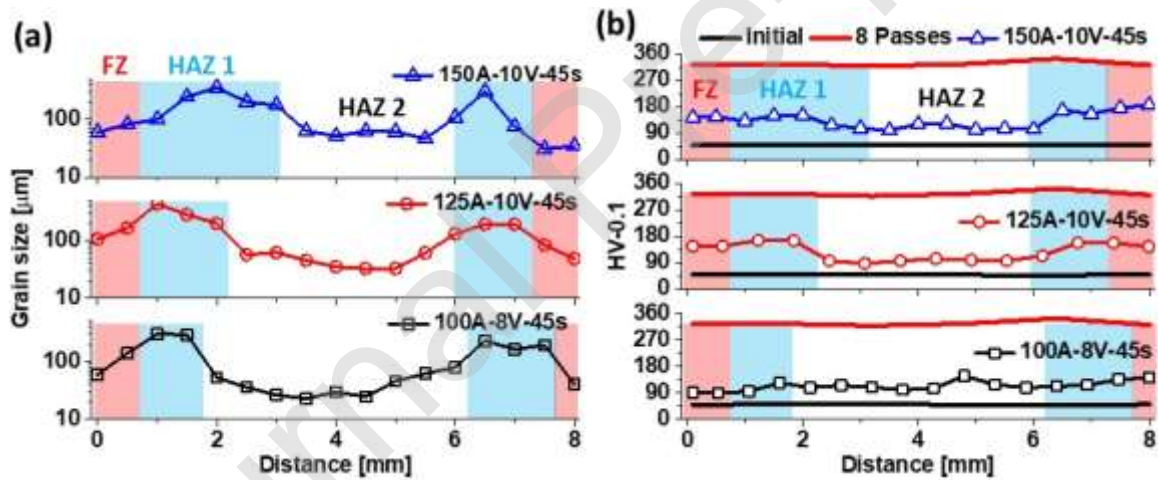**Figure 8.** a) Grain size profiles across the sample diameter, and b) hardness evolution across the sample diameter for the three GTAW conditions.
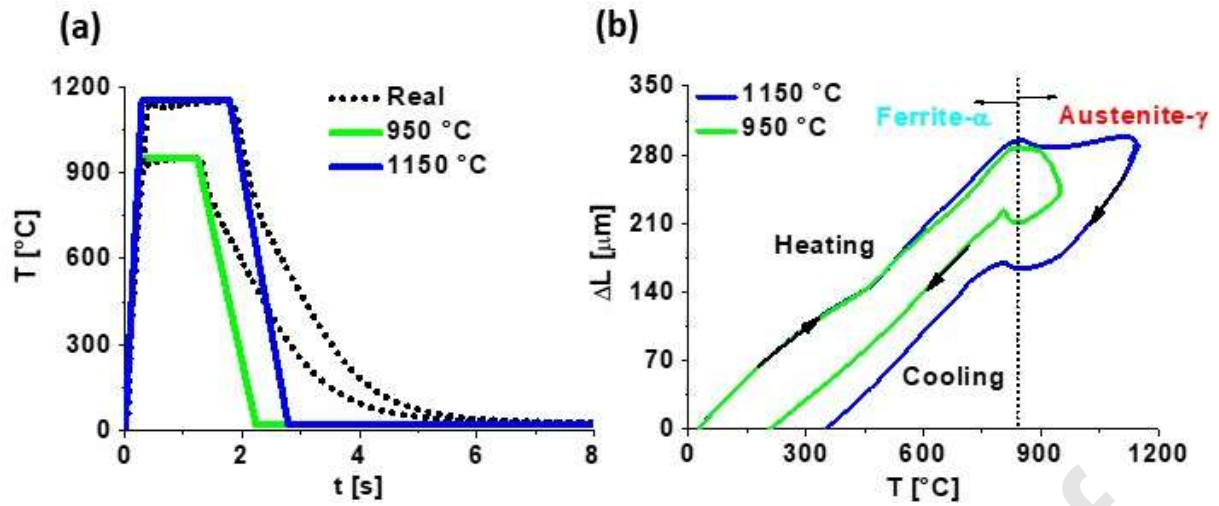
33

Figure 9. Thermal cycles for the 950 ⁰C and 1150 ⁰C heat treatments, and b) dilatometry curves for the two heat treatments.
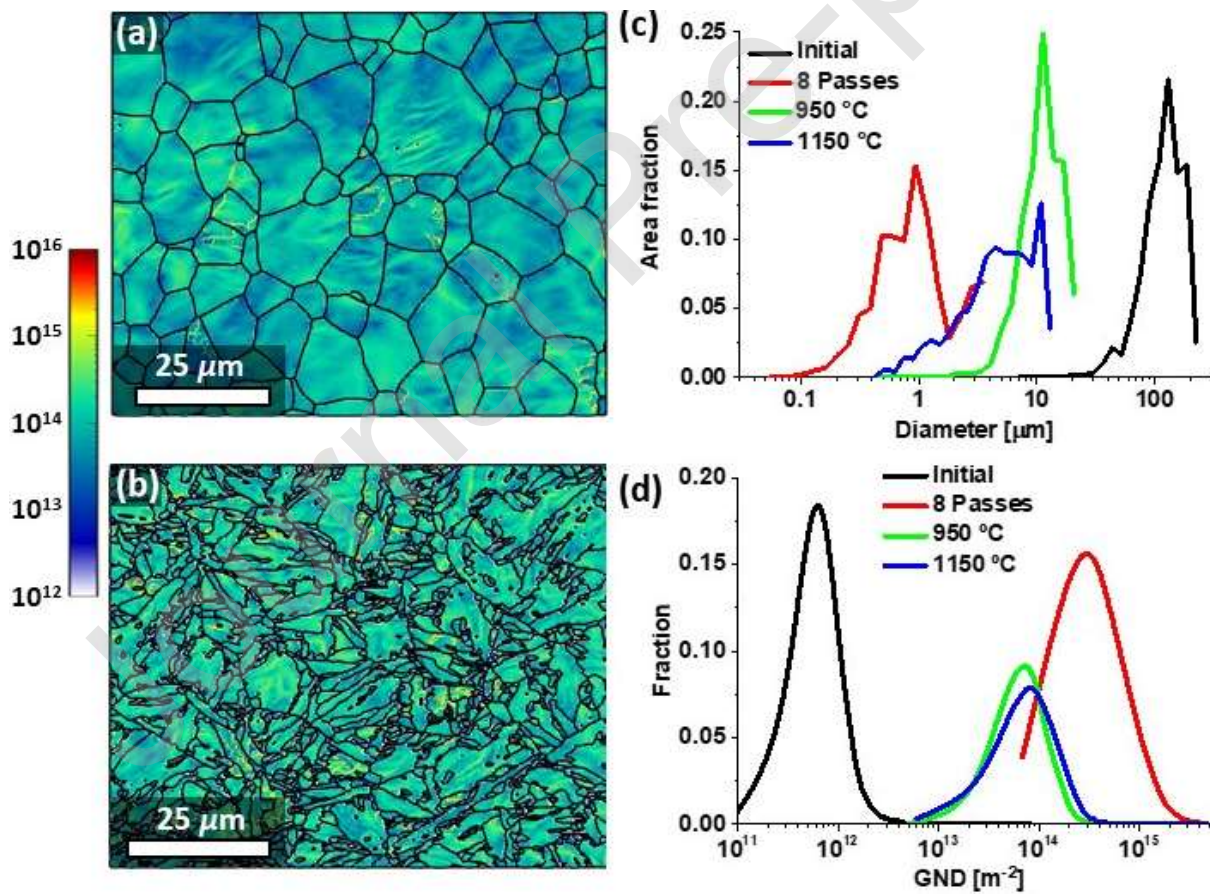

Figure 10. GND maps after the heat treatments, a) 950 ⁰C, b) 1150 ⁰C, c) grain size evolution after the heat treatments, and d) GND distributions.

Table 1. Chemical composition of Armco iron.

Element	C	Si	Mn	P	S	Cr	Mo	Ni	Al	Fe
wt %	0.01	0.01	0.06	<0.01	<0.01	0.02	<0.005	0.038	0.013	Balance

Table 2. Microstructure properties

Condition	Subgrain size [µm]	Grain size [µm]	f_{LAGB}	ρ_{LAGB} [m^{-2}]	$\overline{\gamma}$ [J/m^2]	E_b [J/mol]	σ_{SGB} [MPa]	σ_{GB} [MPa]
Initial	71.3	90.1	0.05	8.53×10^{10}	0.59	0.1	19.2	37
8 Passes	0.3	0.5	0.41	4.25×10^{14}	0.54	24.9	308.3	404.8
950 °C	7.6	8.7	0.36	1.02×10^{13}	0.54	1.0	61.8	97.7
1150 °C	1.6	1.9	0.52	1.26×10^{14}	0.49	4.4	207.4	181.5